Integration of Hard and Soft Supervised Machine Learning for Flood Susceptibility Mapping

Soghra Andaryani[a], **Vahid Nourani** [a], **Ali Torabi Haghighi**[b], **Saskia Keesstra**[c,d]

[a] Center of Excellence in Hydroinformatics, Faculty of Civil Engineering, University of Tabriz, Tabriz, Iran

[b] Water, Energy and Environmental Engineering Research Unit, University of Oulu, 90570 Oulu, Finland

[c] Team Soil, Water and Land Use, Wageningen Environmental Research, Droevendaalsesteeg 3, 6708RC Wageningen, the Netherlands

[d] Civil, Surveying and Environmental Engineering, The University of Newcastle, Callaghan 2308, Australia.

Abstract

Flooding is a destructive natural phenomenon that causes many casualties and property losses in different parts of the world every year. Efficient flood susceptibility mapping (FSM) can reduce the risk of this hazard, and has become the main approach in flood risk management. In this study, we evaluated the prediction ability of artificial neural network (ANN) algorithms for hard and soft supervised machine learning classification in FSM by using three ANN algorithms (multi-layer perceptron (MLP), fuzzy adaptive resonance theory (FART), self-organizing map (SOM)) with different activation functions (sigmoidal (-S), linear (-L), commitment (-C), typicality (-T)). We used these models for predicting the spatial expansion probability of flood events in the Ajichay river basin, northwest Iran. Inputs to the ANN were spatial data on 10 flood influencing factors (elevation, slope, aspect, curvature, stream power index, topographic wetness index, lithology, land use, rainfall, and distance to the river). The FSMs obtained as model outputs were trained and tested using flood inventory datasets earned based on previous records of flood damage in the region for the Ajichay river basin. Model validation was carried out using total operating characteristic (TOC) with an area under the curve (AUC). The highest success rate was found for MLP-S (92.1%) and the lowest for FART-T (75.8%). The projection rate in the validation of FSMs produced by MLP-S, MLP-L, FART-C, FART-T, SOM-C, and SOM-T was found to be 90.1%, 89.6%, 71.7%, 70.8%, 83.8%, and 81.1%, respectively. Sensitivity analysis using one factor-at-a-time (OFAT) and all factors-at-a-time (AFAT) demonstrated that all influencing factors had a

positive impact on modeling to generate FSM, with altitude having the greatest impact and curvature the least.

Keywords: Flood susceptibility map; Artificial neural network; Classification; Total operating characteristic with area under curve; Ajichay river basin-Iran.

1. Introduction

River flooding is one of the most destructive natural hazards, affecting local populations and structures, causing morphological changes by transporting sediment and soil (Mirzaee et al., 2018), damaging agricultural land, and resulting in severe economic losses (Penning-Rowsell et al., 2005; Balica et al., 2009; Talbot et al., 2018). River floods and flash floods arising from severe rain events or sudden snowmelt or dam collapse have been occurring more frequently in recent years, due to climate change (Ardalan et al., 2009; Sharifi et al., 2012; Hosseini et al., 2020).

The global flood risk has increased by more than 40% over the past two decades and may increase further in future due to global climate change and urbanization, with the largest increases in the U.S, Asia, and Europe (Raj and Singh, 2012; Alfieri et al., 2017; Vaghefi et al., 2019). Flooding affected approximately 109 million people worldwide between 1995 and 2015, causing USD 75 billion in damage annually (UNISDR and CRED, 2015). Iran is one of the most vulnerable areas to river flooding in Asia (Sharifi et al., 2012; Vaghefi et al., 2019). Recently (e.g., in 2017 and in April and December 2019), devastating flash floods were experienced in most parts of Iran, causing great financial losses through damage to arable land, bridges, tunnels, and roads and loss of life.

To reduce flood damage, the layout of watershed management measures, e.g., wet ponds and detention dams, and of early flood warning systems needs to be optimized (Zalewski, 2002; Pilon, 2005; Ardalan et al., 2009; Tu et al., 2020). Flood susceptibility mapping (FSM) is an important tool now being widely used for this purpose (Rahmati et al., 2015, Tehrany et al., 2017, Samanta et al., 2018; Tien Bui et al., 2019a; Rahman et al., 2019; Nourani and Andaryani, 2020). Although heavy rainfall is the major cause of flood events in Iran, the hydrological and geomorphological features of river basins also influence flood characteristics, and different basins may exhibit different flood responses to a particular magnitude of rainfall event (NOAA, 2010). Several methods have been used in FSM, e.g., statistical analysis (Faghih et al., 2017), geographical information system (GIS) techniques (Tehrany et al., 2015b), decision tree (Tehrany et al., 2013), multi-criteria decision model (Arabameri et al., 2019; Nourani and Andaryani, 2020), hydrological and hydrodynamic models (Ekeu-wei et al., 2018), and artificial neural network (ANN) models (Tehrany et al., 2015a; Rahmati et al., 2019a; Darabi et al., 2019; Kalantari et al., 2020).

The ANN method has been applied extensively to solve different hydrological issues, e.g., river flow forecasting (Veintimilla-Reyesa et al., 2016), rainfall-runoff modeling (Nourani, 2017), water quality modeling (Elkiran et al., 2019), prediction of suspended sediment load in river (Rajaee et al., 2011), determination of aquifer parameters (Adiat et al., 2020), prediction of salinity in water resources (Nasra and Zahran, 2014), and natural hazard modeling (Tehrany et al., 2015a; Rahmati 2019b). ANN has been shown to be a powerful tool for prediction and is a non-parametric method. However, ANN is a black-box model and the process for optimizing the network involves many iterations to find the weights for each input and number of hidden layers, which is very time-consuming (Savic et al., 1999; Nourani et al., 2014).

There are different ANN algorithms available, e.g., multi-layer perceptron (MLP), self-organizing map (SOM), and fuzzy adaptive resonance theory (FART). MLP is a supervised classifier and simulator via back-propagation, while SOM and FART are both unsupervised and supervised clustering and classifier models. These algorithms have widely been used for land use/cover classification but, to our knowledge, have rarely been applied for FSM. Thus, there is no universal agreement and guidelines on their application for FSM. In the present study, these algorithms (hard and soft supervised forms) were applied with different activation functions (sigmoidal (-S), linear (-L), commitment (-C), typicality (-T)), namely MLP-S, MLP-L, FART-C, FART-T, SOM-C, and SOM-T to provide FSM. The results were presented as a two-class map, showing flood-sensitive and non-flood areas. Flood-sensitive area (flood class) was shown as the probability of flood occurrence with a soft (fuzzy) pattern which varied from 0 to 1. The performance of the models was evaluated using total operating characteristic (TOC) with area under curve (AUC). TOC provides deeper insights than existing popular metrics such as receiver operating characteristic (ROC), kappa, etc., for evaluating land use/land cover projection (see Pontius and Malanson, 2005; Pontius and Kangping, 2014). Finally, based on success rate and prediction rate, the most effective modeling approach for FAM was identified.

2. Data and methods

2.1. Case study

The Ajichay river is one of the longest and most important rivers in Iran, draining a large area to Lake Urmia in the north-west of the country. The area selected here as a case study, the Ajichay river basin, covers an area of 7567 km^2 and is located east of Lake Urmia basin (Fig. 1). Mean annual rainfall in the river basin is 338 mm, evaporation from free water surfaces is 1246 mm, and probable maximum rainfall for one event is 137 mm. The region is classified as semi-arid, based on De Martonn’s climate index. The Ajichay river runs for about 220 km from mountainous terrain in the east to the west, passing through the Vanier valley and across the plain of Tabriz to discharge into Lake Urmia. The river water is used for irrigation on the plain. The city of Tabriz, a number of densely populated rural settlements/urbanization, and many important industrial-commercial businesses and infrastructures have been established along the river (Fig. 1b).

Fig. 1.

2.2. Methods for flood susceptibility

A number of different methods and a total of 10 different influencing factors were employed to provide flood susceptibility maps. Having selected ANN as the method, we evaluated the entire range of 10 influencing factors with regard to their effect on flood occurrence. We used the three types of supervised ANN (MLP, SOM, FART) for network classification in FSM. Fig. 2 depicts the methodology used, which comprised three interrelated stages. The first stage involved collection and preparation of the influencing dataset, based on a flood inventory and available reports about destruction, flood impact factors, and normalizing factors. The second stage was modeling, testing factors of importance (i.e., sensitivity analysis), hard classification by MLP, SOM, and FART, and soft classification by the activation functions (MLP-S, MLP-L, FART-C, FART-T, SOM-C, and SOM-T). In the third stage, the model outputs were categorized into 5 classes (i.e., very low, low, moderate, high, and very high) based on the outcomes of hard and soft classification and the results were calibrated and validated i.e., success and projection rates, respectively.

Fig. 2.

2.3. Data

To develop the land use map, Landsat 5 Thematic Mapper was used. The study area was covered by three frames of Landsat images, with row/path 168-34, 168-33, and 167-34 (Table 1). A digital elevation model (DEM) with 30-m resolution was downloaded from USGS/EarthExplorer (Table 1).

Based on available data (Table 1), we developed two sets of data as the flood inventory, using historical flood records and the influencing factors on flood occurrence.

Table 1. Sources of data used

Data	Source	Date/Scale
Digital elevation model (DEM)	USGS/EarthExplorer	30 m
Land use map	Landsat 5 Thematic Mapper (USGS/EarthExplorer) [1]	30 m
Measured rainfall	IMO and EARW[2]	2002-2015
Geological maps	FRWMO[3]	1:100000
Historical floods	EARW	1999-2017

[1] United States Geological Survey
[2]IMO: Iran Meteorological Organization, EARW: East & West Azerbaijan Regional Water
[3]FRWMO: Forest, Range and Watershed Management Organization-East Azerbaijan (FRWMO)

2.3.1. Flood inventory and training-validation data

Data on historical floods (59 events), collected and reported by East & West Azerbaijan Regional Water (EARW) in 1999, 2005-2012, and 2014-2017, were used for training and validating the models (Fig. 3). The locations of flood events are reported as points, although in the fact the damage around each point might include e.g., 0.5-260 hectares of agricultural land and 0.5-20 hectares of orchards, plus settlements, roads, tunnels, livestock, vehicles, pipes, and casualties (EARW, 1999-2017). Thus, the reported locations of observed floods were used as flood focal points, with each focal point represented by the surrounding three pixels (see Fig. 3). Selection of three pixels for each focal point was based on previous records of flood damage in the region. Each added pixel was examined regarding presence or absence of watershed management installations, e.g., dams, flood control measures, etc., based on field studies, Google-Earth, and EARW reports. A total of 245 pixels were selected for flood-prone areas and 272 pixels for non-flood areas. The non-flood pixels were chosen based on topography by considering height, slope, and hills, which are rarely affected by floods. In the model, a combination of 70% of pixels were used for training and 30% of pixels for validating the model (Fig. 3).

Fig. 3.

2.3.2. Flood influencing factors and preparation

In addition to rainfall, which is the most important influencing factor in flood events, geomorphological, environmental, and geological factors play a crucial role in flooding and inundated area. The 10 main factors influencing flooding are: elevation, slope, aspect, curvature, stream power index (SPI), topographic wetness index (TWI), lithology, land use, rainfall, and distance to river (Tehrany et al., 2017; Rahmati et al., 2019a).

In risk modeling for a particular hazard, here flooding, the spatial correlation between the hazard and the factors influencing it must be considered. In addition, the spatial resolution of all factors used as independent and dependent layers in the training or validation process has to be similar. Therefore, 30×30-pixel resolution (that of the DEM layer) was selected for all factors and training-validation data (Fig. 4). Elevation of the study area is as shown in Fig. 1c. The factors slope, aspect, curvature, river, SPI, and TWI were derived from the DEM.

Each influencing factor must be considered in flood susceptibility mapping. The Tabriz plains area, with lower elevation and little slope, receives more runoff than higher altitudes. Aspect has a different effect on the hydrological regime of the basin in different geographical directions (i.e., cardinal and diagonal directions). For example, on north-facing slopes rainfall is higher and solar radiation is lower than on south-facing slopes. Curvature represents the physical characteristics of the basin in terms of erosion and runoff processes, with negative, positive, and zero values indicating concave, convex, and flat shape of the basin. The slope and its direction (Fig. 4e) in the basin determine the flow rate and direction of the flow, which is accelerated or decelerated due to curvature affects and convergence or divergence. Flood occurrence has a negative correlation with distance from the river (Fig. 4d). Two other influencing factors in flooding are TWI and SPI in the basin. These factors, which are considered geomorphological and hydrological factors, respectively, are calculated as follows:

$$\mathrm{TWI} = \ln\left({A_{sc}}/{\tan\omega}\right) \tag{1}$$

$$\mathrm{SPI} = A_{sc} \times \tan\omega \tag{2}$$

where A_{sc} is specific catchment area (m^2), which is calculated by flow accumulation (i.e., upstream catchment area per pixel in a contour or DEM), and ω is slope gradient based on degree.

SPI shows the power of water on topographic slopes and TWI the amount of cumulative flow at any point (here any pixel) in the basin (Chen and Yu, 2011). There is a linear relationship between TWI and soil moisture, and the magnitude of this factor increases on moving toward the river outlet in the direction of gravity (Grabs et al., 2009).

Fig. 4.

Land use and lithology type can influence the infiltration process and play a major role in runoff generation. Eight types of land use (dryland farming (22.4%), bare soil (2.3%), irrigated wheat (6.5%), orchard (1.3%), weak pasture (64.0%), residential (0.47%), summer crops (2.7%), and water (0.2%)) were derived in the study area, based on Landsat 5 images for August 2007 and using the support vector machine (SVM) method (Fig. 4h). The study area is inherently flood-prone, as the dominant land uses are weak pasture and dryland farming.

Much of the geological area is covered by recent alluvium (22%) and conglomerate-sandstone (20%) (Fig. 4i). A rainfall map was produced based on interpolation of observed rainfall at 29 meteorological stations, using the inverse distance weighted (IDW) method with root mean square error (RMSE) of 0.5, which produces a more reasonable representation than other interpolation techniques (Hsieh et al., 2006). It should be noted that the value 0-1 in Figs. 4a-i is the normalized value of each factor. The real value (e.g., rainfall as continuous data) or class (i.e., land use and lithology as a discrete data) is also shown in the legend of these maps.

2.4. Methods

The three ANN algorithms (MLP, SOM, and FART) were used with the different activation functions to produce FSMs based on observed data and influencing factors. These algorithms can produce the FSM as a hard classification (i.e., two classes, flood and non-flood) or a soft classification (i.e., probability of flood in the range 0 (zero probability of flooding) to 1 (100% probability of flooding) (Umar et al., 2014; Tehrany et al., 2015a)). Producing the FSM as a soft classification map requires the use of functions (here MLP-S, MLP-L, FART-C, FART-T, SOM-C, and SOM-T) to allocate each pixel to each probability class, which is not needed in hard classification. Categorization of FSMs produced by soft classification or other models is necessary for better visual inspection and interpretation (Tehrany et al., 2015a, b; Rahmati et al., 2015; Rahmati et al., 2019a). Here, we rendered the FSMs range as categorical classes (i.e., very low, low, moderate, high, and very high) based on the Jenks Natural Breaks algorithm of ArcGIS.

2.4.1. Multi-layer perceptron (MLP)

Multi-layer perceptron (three or more type layers) can isolate non-linear data, such as the relationship between flood observation data and the influencing dataset, as interrelated factors. In this method, input layer signals are carried by nodes to the next layer in a feed-forward path (Nourani et al., 2014). As the signal is carried on from node to node, it is adjusted by the weight assigned to their contact (Zambri et al., 2015). The weighted signals from all nodes are combined by the receiving node, which is linked to the previous layer. The weight received by a node is calculated as (Nourani et al., 2014):

$$net_j = \sum \omega_{ji} o_i \quad (3)$$

where ω_{ji} represents the weights between node i and node j, and o_i is the output from node i. The output from a given node j is then computed from:

$$o_j = f(net_j) \quad (4)$$

where f is a non-linear sigmoid or linear function which is applied to the weighted sum of the inputs before the signal is passed to the next layer.

Furthermore, the signal forms the network output when it reaches the output layer. In conventional hard classification in which the pixels are only divided into a single class, the output of one node is set to 1, while other nodes in the output layer are equal to zero.

As described above, a training pattern is provided to the network and the signals are fed-forward for the MLP. The network output is then compared with the desired output, such as a series of training data related to known classes and the computed error. Next, this error is back-propagated by the network and the weights of the connections, which are typically set randomly at the beginning, are generally modified based on what is recognized as the generalized delta rule:

$$\Delta\omega_{ji}(n+1) = \eta(\delta_j o_i) + \alpha\Delta\omega_{ji}(n) \quad (5)$$

where η is the learning rate parameter, δ_j is an index measures the rate of change in the error, and α is the momentum parameter. This procedure of feeding forward signals and back-propagating the error is repeated iteratively until the error of the network is minimized or an acceptable magnitude is reached. Additionally, the neural network can learn by modifying the adaptive weights successively. In the present case, the final weights between the acquired layers during training of the ANN and the contribution or significance of each of the 10 elements were utilized to produce the FSM for the study area (Fig. 5a).

2.4.2. Fuzzy Adaptive Resonance Theory (FART)

The concept of FART, which was first introduced by Carpenter et al (1991), set the ground for developing a fuzzy set theory. Within the adaptive resonance theory (ART) family of ANN, FART is one of the most popular models for data classification spatially for land use/cover (Li and Eastman, 2006a). This model includes two ART modules (ARTa and ARTb) bridged by a map field, which can form associative maps between the clusters of input and output domains produced by the ARTa and ARTb modules, respectively (Fig. 5b). Each module encompasses normalization (F0), input (F1), and recognition (F2), layers. FART can be employed as a classifier when the output domain is a finite series of class labels. The algorithm of FART can be simply depicted as follows:

The module ARTa obtains the input pattern and the normalization of an M-dimensional input vector *a* is complement-coded to a 2M-dimensional vector A:

$$\mathrm{A} = (\mathrm{a}, \mathrm{a^c}) = (\mathrm{a}_1, \ldots, \mathrm{a}_\mathrm{M}, 1-\mathrm{a}_1, \ldots, 1-\mathrm{a}_\mathrm{M}) \quad (9)$$

The dimension of the input vector is then kept constant:

$$|\mathrm{A}| = |\mathrm{a}, \mathrm{a}^{\mathrm{c}}| = \sum_{\mathrm{i}=1}^{\mathrm{M}} \mathrm{a}_{\mathrm{i}} + \left(\mathrm{M} - \sum_{\mathrm{i}=1}^{\mathrm{M}} \mathrm{a}_{\mathrm{i}}\right) = \mathrm{M} \tag{10}$$

Next, the input sample **A** selects the category node stored in the network by the category choice function (CCF):

$$\left|A \wedge \omega_j^a\right| / \left|\omega_j^a\right| + \alpha_a = T_j(A) \tag{11}$$

where $\wedge$ is a min operator, α_a is the choice function of ARTa, and ω_j^a is the weight vector of the jth category node.

When a winning category node is selected, a vigilance test, i.e., a similarity check against a vigilance parameter ρ_a of the chosen category node, is performed:

$$\frac{\left|A \wedge \omega_j^a\right|}{|A|} \geq \rho_a \tag{12}$$

where ω_j^a is the winning jth node.

When the above category match function criterion is satisfied, resonance occurs and learning takes place; namely, the weight vector ω_j is updated according to the following equation:

$$\omega_j^{new} = \beta\left(A \wedge \omega_j^{old}\right) + (1 - \beta)\omega_j^{old} \tag{13}$$

where $\beta \in [o, 1]$ indicates the learning rate.

Otherwise, a new node is produced in F_2^a which codes the input pattern. Furthermore, an identical learning algorithm simultaneously occurs for the ARTb module by utilizing the target pattern. The winning node in F_2^a sends a prediction to ARTb by the map field after resonance occurs in ARTa and ARTb. A vigilance test is applied to the map field. Failing the test means that the winning node of ARTa predicts an inappropriate target class in ARTb and a match tracking process initiates accordingly. During match tracking, the value of ρ_a increases until it is slightly higher than

$|A \wedge \omega_j^a||A|^{-1}$. Then, a new search is conducted for the other winning node in ARTa and the process continues until the selected F_2^a node can make an accurate prediction in ARTb.

2.4.3. Self-organizing map method (SOM)

Self-organizing map method is commonly used to picture a high-dimensional space, since it can map extremely non-linear high-dimensional input space in lower-dimensional spaces (normally one or two dimensions) including MLP. With large-scale datasets, reducing the dimensionality is essential to the point where further analysis and exploration is impossible or leads to no new insights. Therefore, given that "dimension reduction of a multivariate dataset" is considered one of the advantages of SOM, it can play a role in providing a reduced-dimension representation for modeling flood inundation spatially. The Euclidean distance (ED) module is utilized to determine the weight of the variables. Further, SOM calculates the ED among the input cells (ʄ) and neurons (M) and seeks the winning neuron (WN) through applying the nearest-neighbor rule. The ED is calculated as:

$$\|ʄ - \mathrm{M}\| = \sqrt{\sum_{i=1}^{n}\left(x_i^p - \omega_{jk,i}\right)^2} \qquad (6)$$

where $ʄ = (ʄ_1, ʄ_2, \dots, ʄ_n)^T$, $M = (M_1, M_2, \dots, M_n)^T$, x_i^p= the ith component of the pth input vector x^p, and $\omega_{jk,i} =$ the weight link of x_i^p and the neuron located at (j, k) of the Kohonen layer.

WN (M) is calculated as:

$$\|ʄ - \mathrm{M}\| = {}^{min}_{\ \ i}\ \|ʄ - \mathrm{M}\| \qquad (7)$$

The SOM updates the weight vector of the unit i using the so-called "self-organization" learning rule as:

$$\omega_{jk,i}(t+1) = \omega_{jk,i}t + a(t)h_{ci}\left(r_{jk}(t)\right)\left[x_i^p(t) - \omega_{jk,i}(t)\right] \quad (8)$$

where t denotes time, $a(t)$ is the learning rate and ranges between [0,1], and $h_{ci}\left(r_{jk}(t)\right)$ is the neighborhood kernel around the winner unit (c) with a neighborhood distance $r_{jk}(t)$.

If a small learning rate is taken, the model will take a very long time to converge. On the other hand, the model may fluctuate and lead to unsteady learning if the learning rate is large, since it may overstep a minimum. In the present study, a constant value of 0.6 was selected for $a(t)$, based on a trade-off between speed and accuracy. The modeling is repeated until the maximum number of iterations (t_{max}) is reached or until the alteration in the weight magnitudes is less than the specified threshold.

The SOM selects incidental amounts for the initial weights, followed by seeking the WN by employing the ED. The neuron which has the highest similarity to the input is selected as the WN in this stage. Finally, SOM tunes the weights of the WN based on the input vector, which results in decreasing the distance of the weights to the WN. This process continues for a vast number of cycles, in order to create a condition for layer unfolding. The SOM includes coarse-tuning (rough-tuning) and fine-tuning phases. The former is an unsupervised clustering learning procedure, while the second is learning vector quantization (LVQ) based on the former phase. The LVQ can be divided as a supervised learning process and implements information for the input set to tune the weight of the output maps (Fig. 5c). In the present study, the SOM model was run for 20,000 training iterations (i.e., 10,000 iterations each in rough-tuning and fine-training phases).

2.4.4. Soft classification by activation function of ANN

To produce an FSM as a soft classification, the fuzzy membership method must be combined with the ANN to explain the flood inundation probability map. In general, fuzzy sets which include various degrees of set membership are evaluated. Fuzzy sets are considered appropriate if the boundaries between the phenomena are not distinct or hard. In neuro-fuzzy methods, the power of neural networks is integrated with the fuzzy logic in order to empower the fuzzy rules for incorporation into the classification and enable the intrinsic uncertainty in classification for representation and minimization. Here, the considered fuzzification activation functions were linear and sigmoid (Karul and Soyupak, 2006) for MLP and commitment (C_i) and typicality (T_i) for FART and SOM, respectively (Li and Eastman, 2006a, 2006b and 2010).

In MLP, a functional relationship between inputs and outputs can be expressed by the two-layer sigmoid/linear network (L_{net_j} *and* S_{net_j} *in Eqs* 9 *and* 10). In soft classification in which the output of one node (i.e., j) is set from 0 to 1 these functions are calculated as:

$$L_{net_j} = net_j \tag{9}$$

$$S_{net_j} = {}^{1}\!/_{1 + e^{-net_j}} \tag{10}$$

In both FART and SOM, the degree of commitment that the models can label as a special class to an input pattern was calculated based on the provoking proportion of the class on its best matching unit as Eq. 11:

$$C_i = {}^{P_i(j)}\!\Big/_{\sum_{i=1}^{n} P_i(j)} \quad , \quad P_i(j) = {}^{f_i(j)}\!/_{N_i} \tag{11}$$

where $P_i(j)$ is the proportion of training site of class i (1, 2, . . ., m) provoking neuron j (1, 2, . . ., n) and $f_i(j)$ is the frequency of neuron j triggered by pixels labeled as class i, and N_i is the total sample number of class i in the training sites (Li and Eastman, 2010).

FART and SOM Typicality unlike commitment measure which accumulates frequency uses the maximum provoking frequency within the underlying class of interest (Eq. 12) (Eastman, 2006a).

$$T_i = {f_i(j)} \Big/ {\max_j\{f_i(j)\}} \qquad (12)$$

Fig. 5.

2.4.5. The sensitivity of models to factors

An initial sensitivity analysis was carried out into the considered approaches by one factor-at-a-time (OFAT) and all factors-at-a-time (AFAT). In OFAT, a single variable is held constant and this is repeated for all variables. In AFAT, all variables are held constant at their mean values except for one, which provides complementary information for each variable. For example, testing a variable on its own indicates an accuracy of 0.4 if its removal decreases the accuracy from 0.7 to 0.5, although this is not frequently the case. However, it relates to the presence of the interaction effects, as well as establishing inter-correlations between the input variables (for more details see Pianosi et al., 2016).

2.4.6. Validation method

The use of TOC (total operating characteristic) and its AUC (area under curve of TOC) is considered one of the most reliable methods to evaluate the efficiency of predicted maps and for change detection (Pontius and Malanson, 2005; Pontius and Kangping, 2014). In addition, TOC-AUC is popular due to its complete, reasonable, and visually understandable procedure in validation of change detection or spatial simulation (Pontius and Kangping, 2014). In this study, the flood probability index obtained was organized in descending order and then divided into 100 categories on the y-axis, with cumulative 1% breaks on the x-axis at seven thresholds. The presence of the flood points (i.e., training and testing) in each class was assessed, and success and prediction rates were obtained accordingly. It should be noted that TOC is formed from four indices, computed based on the value of thresholds (x) a: i) Hits: number of observed flood points with probability more than x, ii) misses: number of observed floods with probability lower than x, iii) correct rejections: number of observed non-flood points with probability more than x, and iv) false alarms: number of observed non-flood points with probability less than x. The R 3.3.3 software and 'TOC package' were used to calculate the indexes (Pontius and Kangping, 2014).

The validation process is performed by overlaying the flood inventory on the derived flood probability index layer. The AUC ranges from 0 to 1, with a value ≤0.5 indicating that the classification is based on chance and a value 1 representing the maximum accuracy, i.e., the method is 100% successful in predicting flood incidence with no error (Pontius and Schneider, 2001; Pontius and Malanson, 2005). Thus, the technique is more reliable if the AUC value is closer to 1. This curve was determined for both success (calibration) and projection (validation) rates; the success rate was obtained by comparison of training data with predicted FSM and the projection rate was achieved by overlaying both testing data and predicted FSM.

3. Results and discussion

3.1. Results of sensitivity analysis

Sensitivity analysis is one of the primary steps before providing of flood susceptibility map that balances the model and recognizes valuable factors in modeling. In the three ANN approaches with different activation functions used here to determine flood-sensitive areas, factors influencing the occurrence of floods (i.e., 10 factors) were selected based on a literature review and the sensitivity of each was analyzed. Fig. 6 shows the results of sensitivity analysis using both the OFAT and AFAT methods.

Based on the OFAT method, elevation and curvature were the most and least effective flood influencing factors, respectively, and the accuracy of the model (initially 84.24%) reached 63.24% and 84.23% without elevation and curvature, respectively (Fig. 6). In other words, when elevation was omitted from the model, the accuracy was reduced by 20%, whereas removing curvature influenced the model accuracy by 0.01%. The lower impact of curvature may be due to the vast area of flat land (value = 0) in the basin (see Fig. 4c). A significant role of elevation in flooding has been reported previously (e.g., Kourgialas and Karatzas, 2011). However, the order of importance of influencing factors can change in different basins due to variations in topographic, geological, and hydrological characteristics. For example, due to the diversity of lithological and topographic features, slope has the potential to be the most effective factor in flood occurrence (Choubin et al., 2019). Furthermore, applying different models for FSM can lead to different rankings of influencing factors (Khosravi et al., 2018; Razavi Termeh et al., 2018).

The ranking of the 10 influencing factors according to the AFAT method was as follows: Elevation (70.17%), rainfall (45.37%), distance to river (69.93%), lithology (63.94%), aspect (53.56%), land-use (59.94%), slope (65.86%), SPI (49.98%), TWI (51.36%), and curvature (50.02%). Thus, elevation was again the most effective factor influencing floods, predicting the FSM with accuracy of 70.17%. When all factors were included in the model the accuracy reached 84.24% (Fig. 6).

Fig. 6.

3.2. Application of ANN algorithms and functions

The different ANN algorithms and flood/non-flood datasets, as well as the different influencing factors, were using in producing a flood potential map. Given that the main purpose of this study was modeling the flood class (the non-flood class was added only due to the structure of the model), only the results for the flood class are discussed. Fig. 7 shows the results of the hard classification, in which there were two classes, as well as part of classes and flood testing data. A better match of the testing data with flood class was achieved with MLP than with the other two ANN algorithms, with all, four, and five testing data located inside the flood class in MLP, FART, and SOM, respectively. This result is in line with the model accuracy reported in section 3.3. In hard classification, an entire class was allocated to flood potential, and it was not clear what percentage of this class was most at risk of flooding. Therefore, soft classification was used to produce the flood susceptibility maps.

Fig. 7.

The range of probability of recognized pixels in the non-flood class in hard classification (i.e., 0-0.5, 0-0.63, 0-0.1, 0-0.01, 0-0.3, and 0-0.15 in MLP-S, MLP-L, FART-C, FART-T, SOM-C, and

SOM-T, respectively) were used as the initial class in soft classification. The remaining probability up to a value of 1.00 (i.e., 0.5-1, 0.63-1, 0.1-1, 0.01-1, 0.3-1, and 0.15-1 for MLP-S, MLP-L, FART-C, FART-T, SOM-C, and SOM-T, respectively) was categorized into five classes (very low, low, moderate, high, and very high flood susceptibility), with equal intervals (Fig. 8). Most studies producing susceptibility maps use equal intervals, to achieve better visualization (Umar et al., 2014; Tehrany et al., 2015a; Khosravi et al., 2018; Tien Bui et al., 2019b). By overlaying the hard classification FSM (see Fig. 7) on the soft FSM, the range of non-flood class for each algorithm or function was defined (see Fig. 8). The range of the non-flood class was not the same with the different algorithms or activation functions, and consequently the range of probability for other classes of flood was different for the different models. Flood susceptibility maps were then created using the six categories (non-flood, and very low, low, moderate, high, and very high flood potential) (Fig. 9).

The maps revealed that the most susceptible pixels to floods (very high class in Fig. 9) were located near the river, based on the river pattern (see Fig. 3). The first flood potential class (very low) was defined as e.g., 0.5-0.6 for MLP-S, 0.01-0.1 for FART-T, or 0.15-0.3 for SOM-T (Fig. 8). Thus, not only a value of 0.0, but also a value of 0.5 (in MLP-S), represented the non-flood class. This shows that combining the results of hard and soft classification of the FSM can lead to better spatial categorization of pixels in the ANN method. The observed discrepancy in probability value for the non-flood class may be due to differences in model performance. For example, the results showed that the typicality function assigned a lower value to the non-flood category than the commitment function in both FART and SOM, confirming findings by Li and Eastman (2006a, 2006b) for land use classification.

Fig. 8.

Fig. 9.

3.3. Validation

The success rate and projection rate of the six flood susceptibility maps were examined and plotted by TOC and AUC. The training and testing data were used to measure success and projection rate, respectively. The TOC graphs were developed based on seven thresholds, and the four TOC indices (hits, misses, correct rejection, and false alarm) were plotted for the fourth threshold (see Fig. 10). Based on TOC, the MLP-S and MLP-L models showed the best performance (Fig. 10). The percentages of false alarm (left side of curve) and hits (under curve) to misses (above curve) and correct rejection (right side of curve) were similar for MLP-S and MLP-L, and thus the AUC value in both models was similar. The accuracy of the FART and SOM activation functions was lower, as seen from the percentages of the TOC indices in Figs. 9c-f. The percentages of hits and correct rejections with TOC were lower for FART and SOM than for MLP, so the models should be tested by several criteria and training data to optimize the accuracy of the values obtained. The FART and SOM models have been extensively used for supervised and unsupervised classification with high accuracy. However, our results showed that FSMs of river basins cannot be accurately sketched when using FART and SOM with limited training data, due to the complex structure and weighting of these models. The efficiency of these two models could be boosted by training them with an enormous amount of observed data, or using them in combination with other methods to produce FSMs.

The AUC results were used to assess success and projection rates (see Fig. 10). Comparing the success rate of the six FSMs obtained using different models (see Fig. 9) revealed that MLP-S was the best method, with the highest success rate (92.1%). It was followed by MLP-L (91.5%), SOM-

C (88.8%), SOM-T (86.1%), FART-C (76.7%), and FART-T (75.8%) (Fig. 10). These results indicate that in both SOM and FART, the commitment function classified the case study with the training data better than the typicality function. The success rate reflects the fit and ability of the model in training with observed flood data, which have already been applied for modeling, so it is necessary to test the projection rate of the model using test data (Tehrany et al., 2015b; Tien Bui et al., 2019b). The highest projection rate produced using AUC was found for MLP-S (90.1%), followed by MLP-L (89.6%), SOM-C (83.8%), SOM-T (81.1%), FART-C (71.7), and FART-T (70.8) (Fig. 10). Therefore, the projection rate results were consistent with the success rate results, and confirmed that the efficiency of flood susceptibility modeling in a region with known flood occurrence was lowest for FART-T. In other words, the success rate and projection rate indicated a powerful fit between observed floods and influencing factors for MLP, but not for FART. Among the activation functions applied in different models, sigmoidal for MLP and commitment for SOM and FART showed the best performance. The results for MLP-S are in line with findings by Özkan and Erbek (2003), Shenouda (2006), and Yonaba et al. (2010), who used MLP with different functions for land use classification and stream flow forecasting. However, the training time for running the models to produce FSMs was shorter for MLP-L. It is worth mentioning that the results of MLP-L were very similar (less than 0.05% difference) to those of MLP-S in producing the FSM. In the other words, the discrepancy of projection rates between the two activation functions (sigmoidal and linear) was negligible, contradicting conclusions by Shenouda (2006), Yonaba et al. (2010), and Zambri et al. (2015). This difference from previous studies may be due to discrepancies in using MLP in different fields, such as land use classification, stream flow forecasting, and renewable energy resources. As mentioned above, the commitment activation function showed the greatest probability of allocating true pixels to the FSM in both SOM and FART.

Li and Eastman (2006a, 2006b) found that using the commitment activation function with FART produced better results than using the typicality function for land use/cover classification, which our results about the functions are consistent with them. They also found that FART-C produced better results than SOM-C, which was contradicted by results in the present study. This difference may relate to the number of training data used, which was much greater for their land use/cover classification (on average 739 training data per class for 101 km^2) than in our observed data (on average 221 training data per class for 7567 km^2).

Overall, based on the accuracy results obtained here for the different ANN algorithms and functions, both MLP-S and MLP-L can be recommended as competent machine learning methods to produce FSM for river basins. Of the two, MLP-S had slightly higher accuracy, but MLP-L was less time-consuming to run.

Fig. 10.

3.4. Recommendations for river management

Risk is a function of two elements: likelihood of an event to take place and the potential damage the event can cause. In the case of flood risk both elements of this equation have changed over the last decades.

The likelihood of flooding has increased due to the changing climate. More erratic and intense rainfall events are expected in many parts of the world due to the higher temperatures that cause the hydrological cycle to change (Shukla et al., 2019). The higher intensity and amounts of rainfall events create more overland flow and associated flooding. Higher rainfall intensities have been recorded in both the lab as well as in the field to create more runoff (Di Prima et al., 2018; Cerda & Rodrigo-Comino, 2020). In addition, land-use changes in the area may increase the amount of surface runoff. Smoother and longer slopes increase the hydrological connectivity of the landscape and increase the amount of water that ends up in the drainage system (Keesstra et al., 2018). These issues were currently not taking into account in this study, but would be useful to be incorporated in a future study.

The other is related to the potential damage of the floods that occur. All over the world flood plain areas are more and more used for industrial and urban build up. Areas that were previously used only for agriculture; or were natural areas are now taking into human use. Therefore, the damages a flood would infer are much larger now, even under unchanged hydrological conditions. Therefore, spatial planning is essential to know which areas are currently under flood risk and how this flood risk will develop under the predicted climate change.

4. Conclusions

This study examined the performance of different artificial neural network approaches (MLP, FART, SOM) in flood susceptibility mapping (FSM), using the case of the Ajichay river basin in northwest Iran. Mapping was based on 10 influencing factors and 221 training and testing data for observed floods in the basin. The importance of influencing factors was tested by OFAT and AFAT. Four types of activation function (sigmoidal (S), linear (L), commitment (C), typicality (T)) were used with the models (MLP-S, MLP-L, FART-C, FART-T, SOM-C, and SOM-T) to create six FSMs. Using the TOC method and its AUC, success rate and the prediction rate were calculated and model performance was compared. The best-performing model was found to be MLP-S, followed closely by MLP-L (success rate 92.1% and 91.5%, respectively). Overall, the results showed that MLP with both activation functions (sigmoidal, linear) can be applied successfully to generate FSMs. MLP-S had slightly higher accuracy, but MLP-L was less time-consuming to run. These results can help spatial land use planning to avoid further increase of flood risk damages.

Acknowledgement

Soghra Andaryani was supported by the Iran's National Elites Foundation (INEF) (grant agreement: 15/7806).

References

Adiat, K. A. N., Ajayi, O. F., Akinlalu A. A., Tijani, I. B., 2020. Prediction of groundwater level in basement complex terrain using artificial neural network: a case of Ijebu-Jesa, southwestern Nigeria. Applied Water Science 10(8). https://doi.org/10.1007/s13201-019-1094-6

Alfieri, L., Bisselink, B., Dottori, F., Naumann, G., Roo, A.D., Salamon, P., Wyser, K., Feyen, L., 2017. Global projections of river flood risk in a warmer world. Earth's Future 5(2), 171-182.

Arabameri, A., Rezaei, K., Cerdà, A., Conoscenti, C., Kalantari, Z., 2019. A comparison of statistical methods and multi-criteria decision making to map flood hazard susceptibility in Northern Iran. Sci. Total Environ. 660, 443–458. https://doi.org/10.1016/j.scitotenv.2019.01.021

Ardalan, A., Holakouie Naieni, K., Kabir, MJ., Zanganeh, AM., Keshtkar, AA., Honarvar, MR., Khodaie, H., Osooli, M., 2009. Evaluation of Golestan province's early warning system for flash floods, Iran, 2006–7. International Journal of Biometeorology 53, 247–254.

Balica, SF., Douben, N., Wright, NG., 2009. Flood vulnerability indices at varying spatial scales. Water Science and Technology 60(10), 2571–2580.

Cerdà, A., Rodrigo-Comino, J., 2020. Is the hillslope position relevant for runoff and soil loss activation under high rainfall conditions in vineyards? Ecohydrol. Hydrobiol. 20, 59–72. https://doi.org/10.1016/j.ecohyd.2019.05.006

Chen, C.Y., Yu, F.C., 2011. Morphometric analysis of debris flows and their source areas using GIS. Geomorphology 129(3-4), 387–397.

Choubin, B., Moradi, E., Golshan, M., Adamowski, J., Sajedi-Hosseini, F., Mosavi, A., 2019. An Ensemble prediction of flood susceptibility using multivariate discriminant analysis, classification and regression trees, and support vector machines. Science of The Total Environment 651, 2087-2096.

Darabi, H., Choubin, B., Rahmati, O., Haghighi, A.T., Pradhan, B., Kløve B., 2019. Urban flood risk mapping using the GARP and QUEST models: A comparative study of machine learning techniques. Journal of hydrology 569, 142-154.

Di Prima, S., Concialdi, P., Lassabatere, L., Angulo-Jaramillo, R., Pirastru, M., Cerdà, A., Keesstra, S., 2018. Laboratory testing of Beerkan infiltration experiments for assessing the role of soil sealing on water infiltration. Catena 167, 373–384. https://doi.org/10.1016/j.catena.2018.05.013

Ekeu-wei, I.T., Blackburn, G.A., 2018. Applications of Open-Access Remotely Sensed Data for Flood Modelling and Mapping in Developing Regions. Hydrology 5, 39.

Elkiran, G., Nourani, V., Abba, SI., 2019. Multi-step ahead modelling of river water quality parameters using ensemble artificial intelligence-based approach. Journal of Hydrology 577, 123962.

Faghih, M., Mirzaei, M., Adamowski, J., Lee, J., El-Shafie, A., 2017. Uncertainty estimation in flood inundation mapping: An application of Non-parametric bootstrapping. River Research and Applications 33(4), 611–619.

Grabs, T., Seibert, J., Bishop, K., Laudon, H., 2009. Modeling spatial patterns of saturated areas: A comparison of the topographic wetness index and a dynamic distributed model. Journal of Hydrology 373(1-2), 15–23.

Hosseini, F.S., Choubin, B., Mosavi, A., Nabipour, N., Shamshirband, S., Darabi, H., Haghighi, A.T., 2020. Flash-flood hazard assessment using ensembles and Bayesian-based machine learning models: Application of the simulated annealing feature selection method. Science of The Total Environment 711, 135161.

Hsieh, H. H., Cheng, S. J., Liou, J. Y., Chou, S. C., Siao, B. R., 2006. Characterization of spatially distributed summer daily rainfall, Journal of Chinese Agricultural Engineering 52, 47–55.
http://www.meted.ucar.edu/communities/hazwarnsys/ffewsrg/FF_EWS.pdf

Karul, C., Soyupak, S., 2006. A comparison between neural network based and multiple regression models for Chlorophyll-a estimation. In Recknagel, F. (ed), Ecological Informatics (Berlin: Springer).

Keesstra, S., Nunes, J.P., Saco, P., Parsons, T., Poeppl, R., Masselink, R., Cerdà, A., 2018. The way forward: Can connectivity be useful to design better measuring and modelling schemes for water and sediment dynamics? Sci. Total Environ. 644, 1557–1572. https://doi.org/10.1016/j.scitotenv.2018.06.342

Khosravi, K., Panahi, M., Golkarian, A., Keesstra, S.D., Saco, P.M., Bui, D.T., Lee, S., 2020. Convolutional neural network approach for spatial prediction of flood hazard at national scale of Iran. J. Hydrol. 591. https://doi.org/10.1016/j.jhydrol.2020.125552

Khosravi, K., Pham, B.P., Chapi, K., Shirzadi, A., Shahabi, H., Revhaug, I., Prakash, I., Bui, D.T., 2018. A comparative assessment of decision trees algorithms for flash flood susceptibility modeling at Haraz watershed, northern Iran. Science of the Total Environment 627, 744–755.

Kourgialas, N.N., and Karatzas, G.P., 2011. Flood management and a GIS modelling method to assess flood-hazard areas—a case study, Hydrological Sciences Journal 56:2, 212-225.

Li, Z., Eastman, J.R., 2006a. Commitment and Typicality Measurements for Fuzzy ARTMAP Neural Network. Proc. SPIE 6420, Geoinformatics 2006: Geospatial Information Science, 64201I (28 October 2006); https://doi.org/10.1117/12.712998.

Li, Z., Eastman, J.R., 2006b. Soft classification algorithms for the Self-Organizing Map. RSSG Student Honor Paper Competition, AAG 2006 Annual Meeting, Chicago, PA, March 7–11, 2006.

Li, Z., Eastman, J.R., 2010. Commitment and typicality measures for the Self-Organizing Map. International Journal of Remote Sensing 31:16, 4265-4280.

Mirzaee, S., Yousefi, S., Keesstra, S., Pourghasemi, H.R., Cerdà, A., Fuller, I.C., 2018. Effects of hydrological events on morphological evolution of a fluvial system. J. Hydrol. 563, 33–42. https://doi.org/10.1016/j.jhydrol.2018.05.065

Nasra, M., Zahran, Z.F., 2014. Using of pH as a tool to predict salinity of groundwater for irrigation purpose using artificial neural network. The Egyptian Journal of Aquatic Research 40(2), 111-115.

NOAA., 2010. Flash Flood Early Warning System Reference Guide. National Oceanic and Atmospheric Administration, U.S. Department of Commerce. Available at:

Nourani, V., 2017. An emotional ANN (EANN) approach to modeling rainfall-runoff process. Journal of Hydrology 544, 267-277.

Nourani, V., Andaryani, Soghra., 2020. Flood Susceptibility Mapping in Densely Populated Urban Areas Using Mcdm and Fuzzy Techniques. IOP Conference Series: Earth and Environmental Science 491 (1), 012003.

Nourani, V., Pradhan, B., Ghaffari, H., Seyed Saber Sharifi., 2014. Landslide susceptibility mapping at Zonouz Plain, Iran using genetic programming and comparison with frequency ratio, logistic regression, and artificial neural network models. Natural Hazards 71, 523–547.

Özkan, C., Erbek, F.S., 2003. The Comparison of Activation Functions for Multispectral Landsat TM Image Classification. Photogrammetric Engineering & Remote Sensing 69 (11), 1225–1234.

Penning-Rowsell, E., Floyd, P., Ramsbottom, D., Surendran, S., 2005. Estimating injury and loss of life in floods: a deterministic framework. Natural Hazards 36(1–2):43–64.

Pianosi, F., Beven, K., Freer, J., Hall, J.W., Rougier, J., Stephenson, D.B., Wagener, T., 2016. Sensitivity analysis of environmental models: A systematic review with practical workflow. Environmental Modelling & Software 79, 214-232.

Pilon, P.J., 2005. Guidelines for reducing flood losses. United Nations.

Pontius Jr, R.G., Kangping, Si., 2014. The total operating characteristic to measure diagnostic ability for multiple thresholds. International Journal of Geographical Information Science 28:3, 570-583.

Pontius Jr, R.G., Malanson, J., 2005. Comparison of the structure and accuracy of two land change models. International journal of Geographical Information Science 19, 243-265.

Pontius, R. G. Jr. Schneider, L., 2001. Land-use change model validation by a ROC method for the Ipswich watershed, Massachusetts, USA. Agriculture, Ecosystems & Environment 85(1-3), 239-248.

Rahman, M., Ningsheng, C., Islam, M. M., Dewan, A., Iqbal, J., Washakh, R. M. A., Shufeng, T., 2019. Flood Susceptibility Assessment in Bangladesh Using Machine Learning and Multi-criteria Decision Analysis. Earth Systems and Environment. doi:10.1007/s41748-019-00123-y

Rahmati, O., Darabi, H., Haghighi, A.T., Stefanidis, S., Kornejady, A., Nalivan, O.A., Bui, D.T., 2019a. Urban Flood Hazard Modeling Using Self-Organizing Map Neural Network. Water 11(11), 2370.

Rahmati, O., Yousefi, S., Kalantari, Z., Uuemaa, E., Teimurian, T., Keesstra, S., Pham, T.D., Bui, D.T., 2019b. Multi-hazard exposure mapping using machine learning techniques: A case study from Iran. Remote Sens. 11. https://doi.org/10.3390/rs11161943

Rahmati, O., Zeinivand, H., Besharat, M., 2015. Flood hazard zoning in Yasooj region, Iran, using GIS and multi-criteria decision analysis. Geomatics, Natural Hazards and Risk, DOI: 10.1080/19475705.2015.1045043

Raj, B., Singh, O., 2012. Study of Impacts of Global Warming on Climate Change: Rise in Sea Level and Disaster Frequency. Global Warming - Impacts and Future Perspectives. doi:10.5772/50464

Rajaee, T., Nourani, V., Zounemat-Kermani, M., Kisi, O., 2011. River suspended sediment load prediction: application of ANN and wavelet conjunction model. Journal of Hydrologic Engineering 16 (8), 613-627.

Razavi Termeh, S.V., Kornejady, A., Pourghasemi, H.R., Keesstra, S., 2018. Flood susceptibility mapping using novel ensembles of adaptive neuro fuzzy inference system and metaheuristic algorithms. Science of the Total Environment 615, 438–451.

Samanta, S., Pal, D. K., Palsamanta, B., 2018. Flood susceptibility analysis through remote sensing, GIS and frequency ratio model. Applied Water Science 8, 66.

Savic, D.A., Walters, G.A., Davidson, J., 1999. A genetic programming approach to rainfall–runoff modeling. Water Resource Management 13(3), 219–231.

Sharifi, F., Samadi, S.Z., Wilson, C.A.M.E., 2012. Causes and consequences of recent floods in the Golestan catchments and Caspian Sea regions of Iran. Natural Hazards 61, 533–550.

Shenouda, A., 2006. A quantitative comparison of different MLP activation functions in classification. In third International Symptom Neural Networks, ISNN 2006, LNCS 3971, 849–857.

Shukla, P. R., Skea, J., Calvo Buendia, E., Masson-Delmotte, V., Pörtner, H. O., Roberts, D. C., ... & Ferrat, M. IPCC, 2019: Climate Change and Land: an IPCC special report on climate change, desertification, land degradation, sustainable land management, food security, and greenhouse gas fluxes in terrestrial ecosystems.

Talbot, C.J., Bennett, E.M., Cassell, K., Hanes, M.D., Minor, E.C., Paerl, H., Raymond, P.A., Vargas, R.V., Vidon, P.G., Wollheim, W., Xenopoulos, M.A., 2018. The impact of flooding on aquatic ecosystem services. Biogeochemistry 141, 439–461.

Tehrany, M. S., Pradhan, B., Jebur, M. N., 2013. Spatial prediction of flood susceptible areas using rule-based decision tree (DT) and a novel ensemble bivariate and multivariate statistical models in GIS. Journal of Hydrology, 504, 69–79.

Tehrany, M. S., Pradhan, B., Jebur, M. N., 2015a. Flood susceptibility analysis and its verification using a novel ensemble support vector machine and frequency ratio method. Stochastic Environmental Research and Risk Assessment 29(4), 1149–1165.

Tehrany, M. S., Pradhan, B., Mansor, S., Ahmad, N., 2015b. Flood susceptibility assessment using GIS-based support vector machine model with different kernel types. Catena 125, 91–101.

Tehrany, M. S., Shabani, F., Neamah Jebur, M., Hong, H., Chen, W., Xie, X., 2017. GIS-based spatial prediction of flood prone areas using standalone frequency ratio, logistic regression, weight of evidence and their ensemble techniques. Geomatics, Natural Hazards and Risk 8(2), 1538-1561.

Tien Bui, D., Tsangaratos, P., Ngo, P.T.T., Pham, T.D., Pham, B.T., 2019b. Flash flood susceptibility modeling using an optimized fuzzy rule-based feature selection technique and tree-based ensemble methods. Science of the Total Environment 668, 1038–1054.

Tien Bui, D.T., Khosravi, K., Shahabi, H., Daggupati, P., Adamowski, J. F., Melesse, M. A., … Lee, S., 2019a. Flood Spatial Modeling in Northern Iran Using Remote Sensing and GIS: A Comparison between Evidential Belief Functions and Its Ensemble with a Multivariate Logistic Regression Model. Remote Sensing 11(13), 1589.

Tu, H., Wang, X., Zhang, W., Peng, H., Ke, Q., Chen, X., 2020. Flash Flood Early Warning Coupled with Hydrological Simulation and the Rising Rate of the Flood Stage in a Mountainous Small Watershed in Sichuan Province, China. Water 12(1), 255.

Umar, Z., Pradhan, B., Ahmad, A., Jebur, M.N., Tehrany, M.S., 2014. Earthquake induced landslide susceptibility mapping using an integrated ensemble frequency ratio and logistic regression models in West Sumatera Province, Indonesia. Catena 118, 124–135.

UNISDR, and CRED., 2015. The Human Cost of Weather-Related Disasters 1995–2015, United Nations Office for Disaster Risk Reduction (UNISDR) and Centre for Research on the Epidemiology of Disasters (CRED), Geneva, Switz.

Vaghefi, S., A., Keykhai, M., Jahanbakhshi, F., Sheikholeslami, J., Ahmadi, A., Yang, H., Abbaspour, K.C., 2019. The future of extreme climate in Iran. Scientific Reports 9(1). doi:10.1038/s41598-018-38071-8

Veintimilla-Reyesa, J., Cisneros, F., Vanegas, P., 2016. Artificial Neural Networks Applied to Flow Prediction: A Use Case for the Tomebamba River. Procedia Engineering 162, 153-161.

Yonaba, H., Anctil, F., Fortin, V., 2010. Comparing Sigmoid Transfer Functions for Neural Network Multistep Ahead Streamflow Forecasting. Journal of Hydrologic Engineering 15 (4), 275-283.

Zalewski, M., 2002. Ecohydrology-the use of ecological and hydrological processes for sustainable management of water resources. Hydrological Sciences Journal 47(5), 823–832.

Zambri, N.A., Mohamed, A., Wanik, M.Z.W., 2015. Performance comparison of neural networks for intelligent management of distributed generators in a distribution system. Electrical Power and Energy Systems 67, 179-190.

Fig. 1. Location of the study area, (a) Lake Urmia basin, and (b) map of the Ajichay river basin showing elevation, population density, location of rain gauges, and downstream position of the city of Tabriz.

Fig. 2. Overview of the methodology applied in this study. DEM: digital elevation model, SPI: stream power index, TWI: topographic wetness index, ANN: artificial neural network, MLP-S: multi-layer perceptron-sigmoidal, MLP-L: multi-layer perceptron-linear, FART-C: fuzzy adaptive resonance theory-commitment, FART-T: fuzzy adaptive resonance theory-typicality, SOM-C: self-organizing map-commitment, SOM-T: self-organizing map-typicality, FSM: flood susceptibility map, TOC: total operating characteristic, AUC: area under curve.

Fig. 3. Flood and non-flood location map used for model training and validation, and (enlarged images) examples of surrounding pixels showing flood and non-flood locations.

Fig. 4. Thematic maps showing flood influencing factors in Ajichay river basin. (a) Mean annual rainfall, (b) aspect, (c) curvature (d) DR: distance to river network, (e) slope in percent, (f) SPI: stream power index, (g) TWI: topographic wetness index, (h) land use, and (i) lithology. Lithology is defined as: AV (acidic-volcanic), A (andesite), CS (conglomerate-sandstone), D (dacite), DM (diorite-monzonite), HZ (hydrothermal zones), I (ignimbrite), LD (lacustrine deposits), LA (latite-andesite), LD2 (lava-dacitic), LF (lava flows), L (limestone), MS (marl-siltstone), NS (nepheline syenite), PL (porphyritic), RA (recent alluvium), LM (limestone-marl), SF (salt flat), TS (tuff-sandstone), and VC (volcano-conglomerate).

Fig. 5. Architecture of using artificial neuron network (ANN) algorithms with different activation layers. (a) Multi-layer perceptron (MLP) with five neurons in the hidden layer, (b) fuzzy adaptive resonance theory (FART) with 20 neurons in F1 and 1452 neurons in F2, with two map fields, and (c) self-organizing map (SOM) with 15×15 neurons in the Korhonen layer. In the equations in (a) and (c), C = commitment activation function, T = typicality activation function, and $f_i(j)$ = frequency of neuron j triggered by pixels labeled as class i (see Li and Eastman, 2006a, 2006b, 2010, for details of equations).

Fig. 6. Results of model sensitivity analysis using one factor-at-a-time (OFAT) and all factors-at-a-time (AFAT) (DR: distance to river, SPI: stream power index, TWI: topographic wetness index).

Fig. 7. Flood susceptibility map based on hard classification using: (a) multi-layer perceptron (MLP), (b) fuzzy adaptive resonance theory (FART), and (C) self-organizing map (SOM). The enlarged images show the match between observed flooding and the results of hard classification.

Fig. 8. Range of flood probability (p) in different non-flood/flood classes when using different artificial neural network algorithms and activation functions for flood susceptibility mapping (FSM). MLP-S: multi-layer perceptron-sigmoidal, MLP-L: multi-layer perceptron-linear, FART-C: fuzzy adaptive resonance theory-commitment, FART-T: fuzzy adaptive resonance theory-typicality, SOM-C: self-organizing map-commitment, SOM-T: self-organizing map-typicality

Fig. 9. Flood susceptibility maps based on soft classification using the models: (a) multi-layer perceptron-sigmoidal (MLP-S), (b) MLP-linear (MLP-L), (c) fuzzy adaptive resonance theory-commitment (FART-C), (d) FART-typicality (FART-T), (e) self-organizing map-commitment (SOM-C), and (f) SOM-typicality (SOM-T).

Fig. 10. Total operating characteristics (TOC) curve and AUC (area under curve of TOC) for the models: (a) multi-layer perceptron-sigmoidal (MLP-S), (b) MLP-linear (MLP-L), (c) fuzzy adaptive resonance theory-commitment (FART-C), (d) FART-typicality (FART-T), (e) self-organizing map-commitment (SOM-C), and (f) SOM-typicality (SOM-T). SR = Success rate and PR = projection rate.

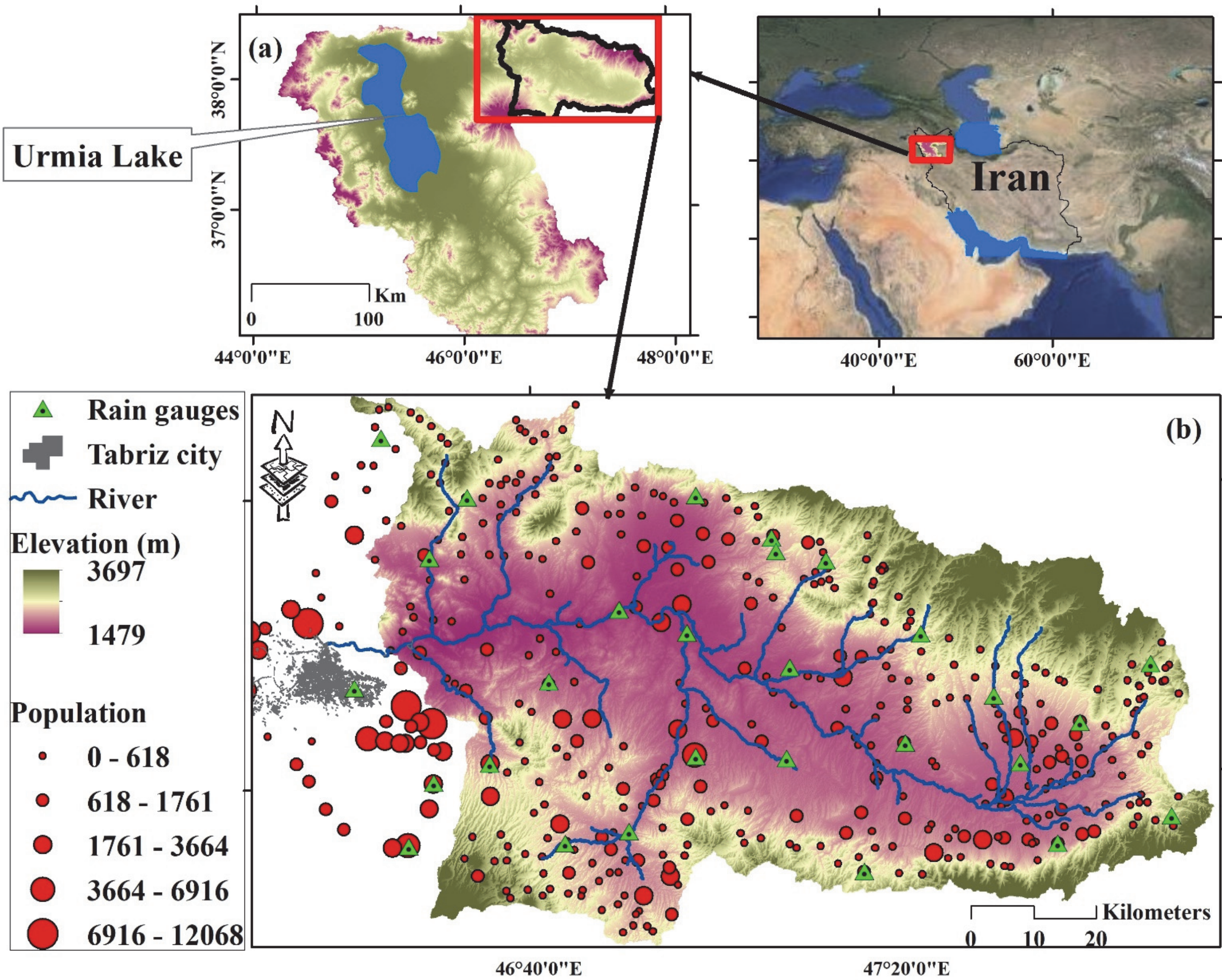
(a)
Urmia Lake
38°0'0"N
37°0'0"N
Km
0
100
44°0'0"E
46°0'0"E
48°0'0"E
Iran
45°0'0"N
37°0'0"N
27°0'0"N
40°0'0"E
60°0'0"E
Rain gauges
Tabriz city
River
Elevation (m)
3697
1479
Population
0 - 618
618 - 1761
1761 - 3664
3664 - 6916
6916 - 12068
(b)
N
38°20'0"N
37°55'0"N
Kilometers
0
10
20
46°40'0"E
47°20'0"E

Fig. 1.

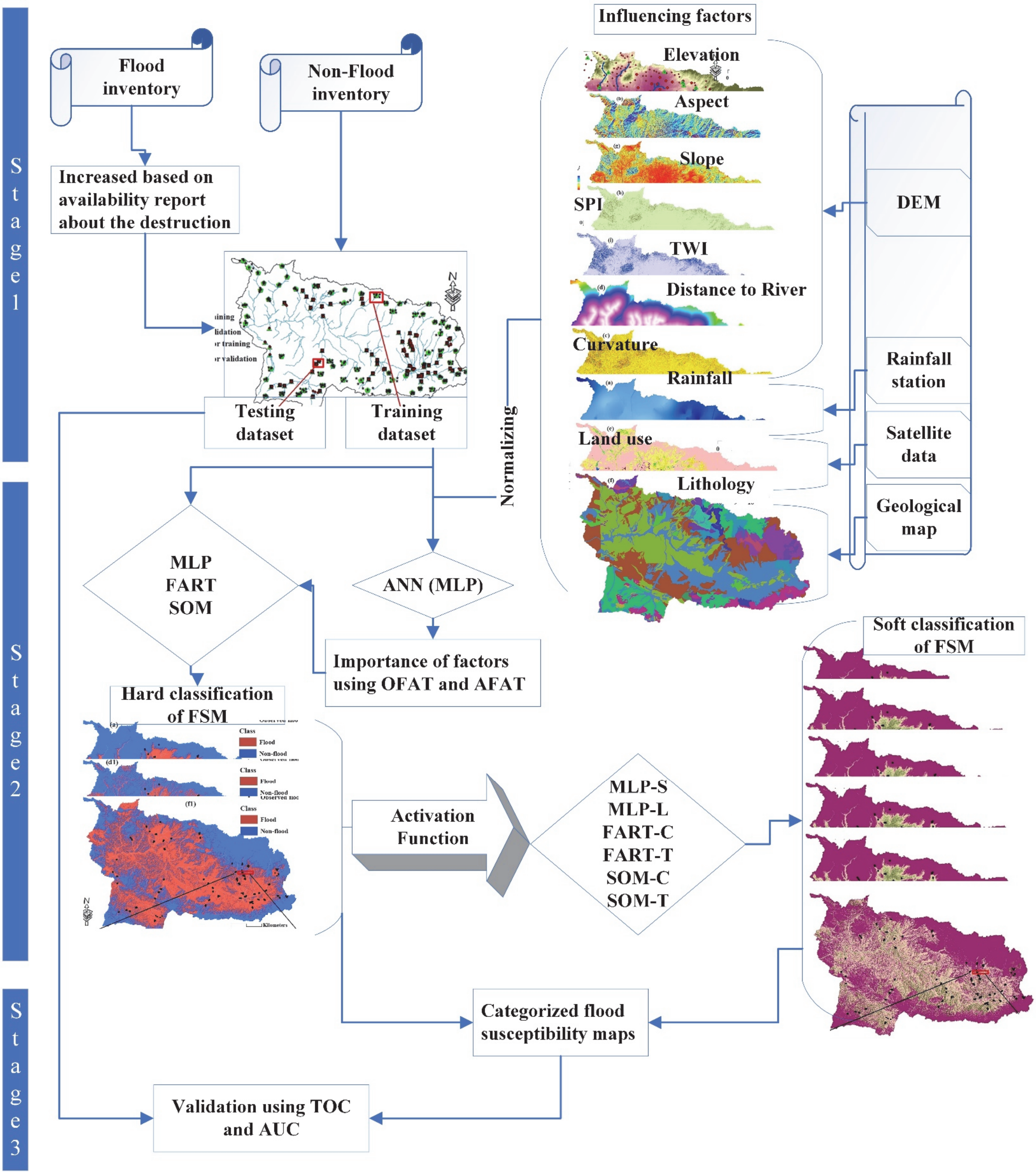
Stage 1
Stage 2
Stage 3
Flood inventory
Non-Flood inventory
Increased based on availability report about the destruction
Testing dataset
Training dataset
Influencing factors
Elevation
Aspect
Slope
SPI
TWI
Distance to River
Curvature
Rainfall
Land use
Lithology
DEM
Rainfall station
Satellite data
Geological map
Normalizing
MLP
FART
SOM
ANN (MLP)
Importance of factors using OFAT and AFAT
Hard classification of FSM
Class
Flood
Non-flood
Activation Function
MLP-S
MLP-L
FART-C
FART-T
SOM-C
SOM-T
Soft classification of FSM
Categorized flood susceptibility maps
Validation using TOC and AUC

Fig. 2.

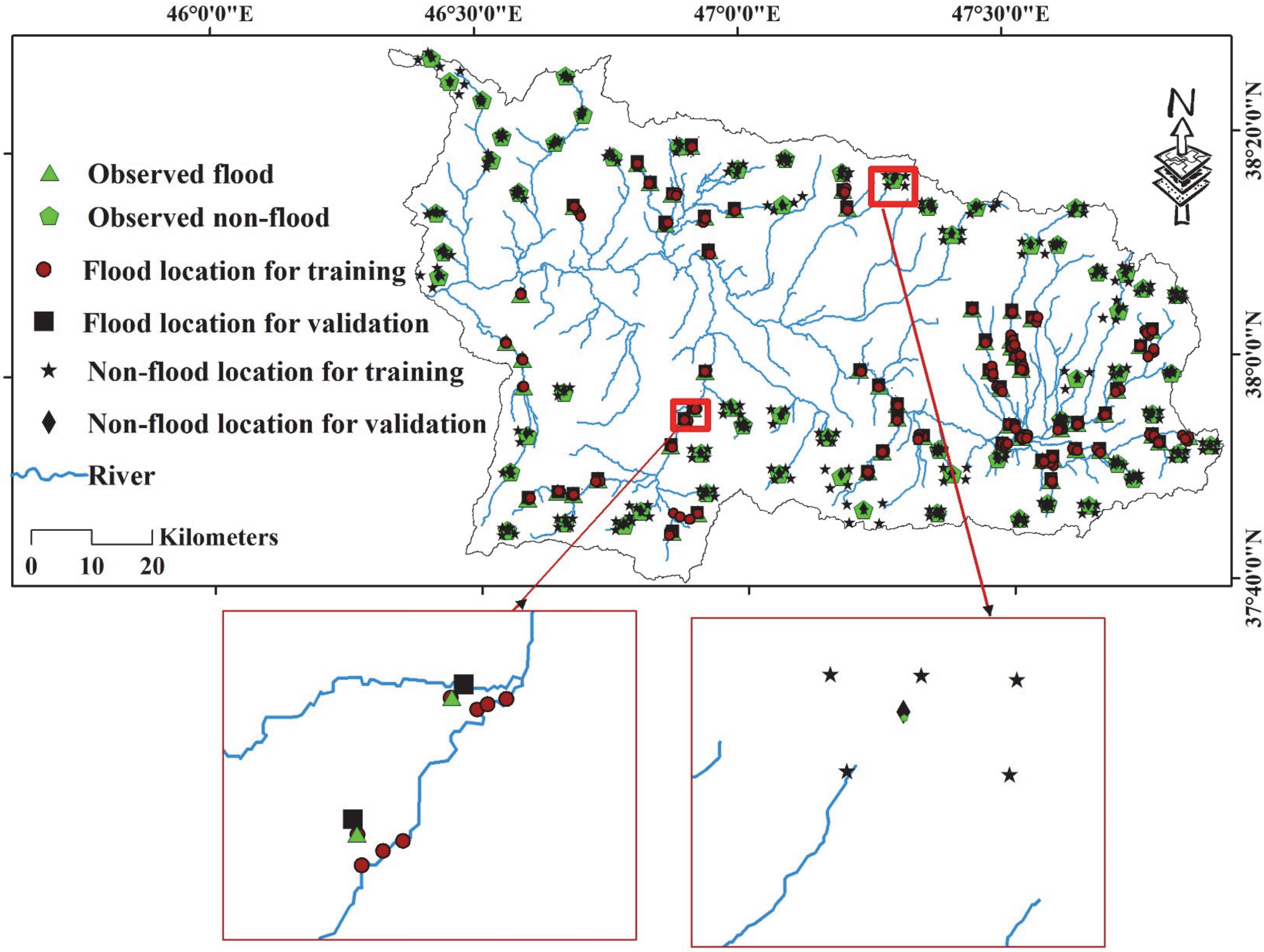
46°0'0"E
46°30'0"E
47°0'0"E
47°30'0"E
38°20'0"N
38°0'0"N
37°40'0"N
Observed flood
Observed non-flood
Flood location for training
Flood location for validation
Non-flood location for training
Non-flood location for validation
River
Kilometers
0
10
20

Fig. 3.

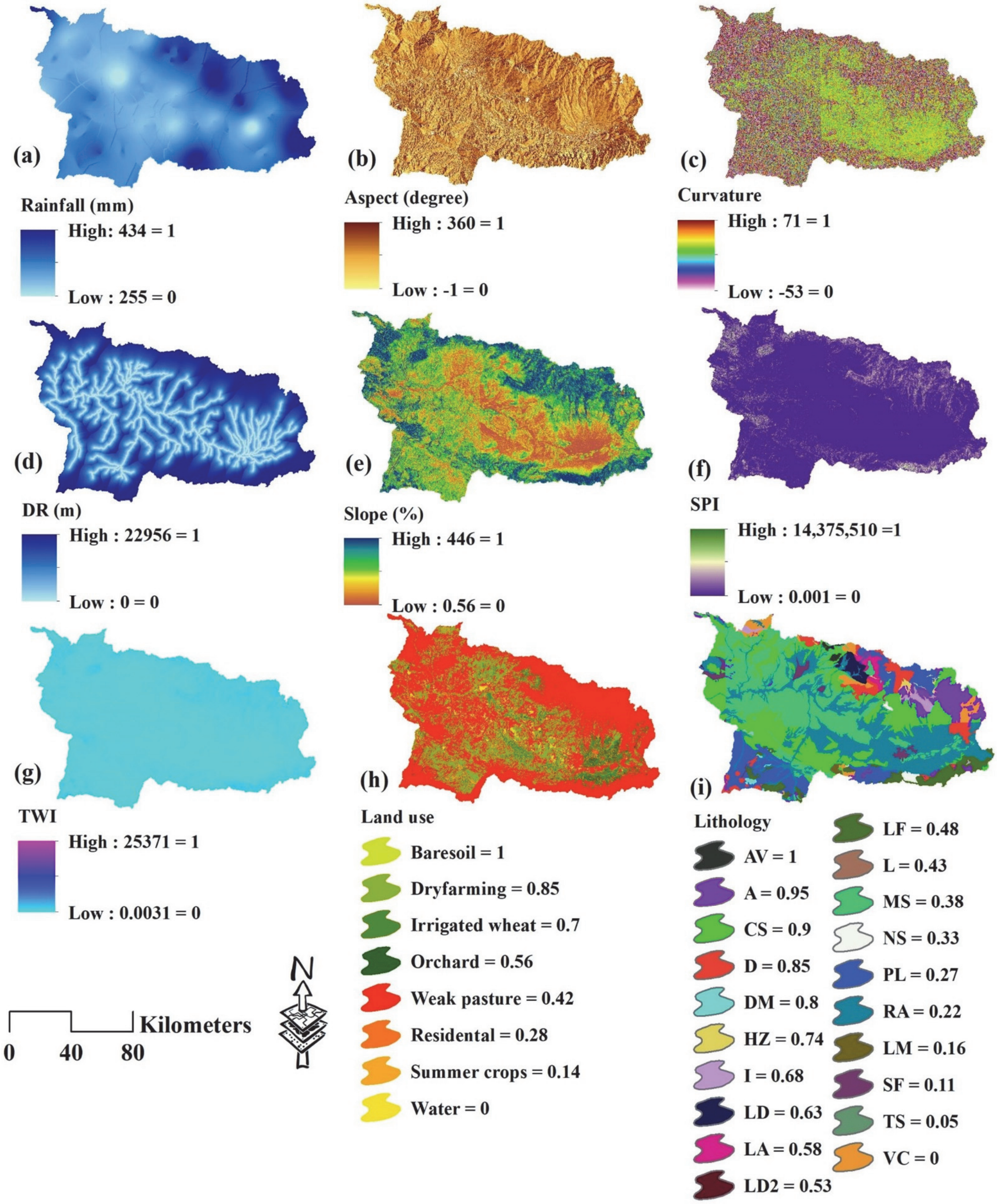
(a)
Rainfall (mm)
High: 434 = 1
Low : 255 = 0
(b)
Aspect (degree)
High : 360 = 1
Low : -1 = 0
(c)
Curvature
High : 71 = 1
Low : -53 = 0
(d)
DR (m)
High : 22956 = 1
Low : 0 = 0
(e)
Slope (%)
High : 446 = 1
Low : 0.56 = 0
(f)
SPI
High : 14,375,510 =1
Low : 0.001 = 0
(g)
TWI
High : 25371 = 1
Low : 0.0031 = 0
(h)
Land use
Baresoil = 1
Dryfarming = 0.85
Irrigated wheat = 0.7
Orchard = 0.56
Weak pasture = 0.42
Residental = 0.28
Summer crops = 0.14
Water = 0
(i)
Lithology
AV = 1
A = 0.95
CS = 0.9
D = 0.85
DM = 0.8
HZ = 0.74
I = 0.68
LD = 0.63
LA = 0.58
LD2 = 0.53
LF = 0.48
L = 0.43
MS = 0.38
NS = 0.33
PL = 0.27
RA = 0.22
LM = 0.16
SF = 0.11
TS = 0.05
VC = 0
N
0
40
80
Kilometers

Fig. 4.

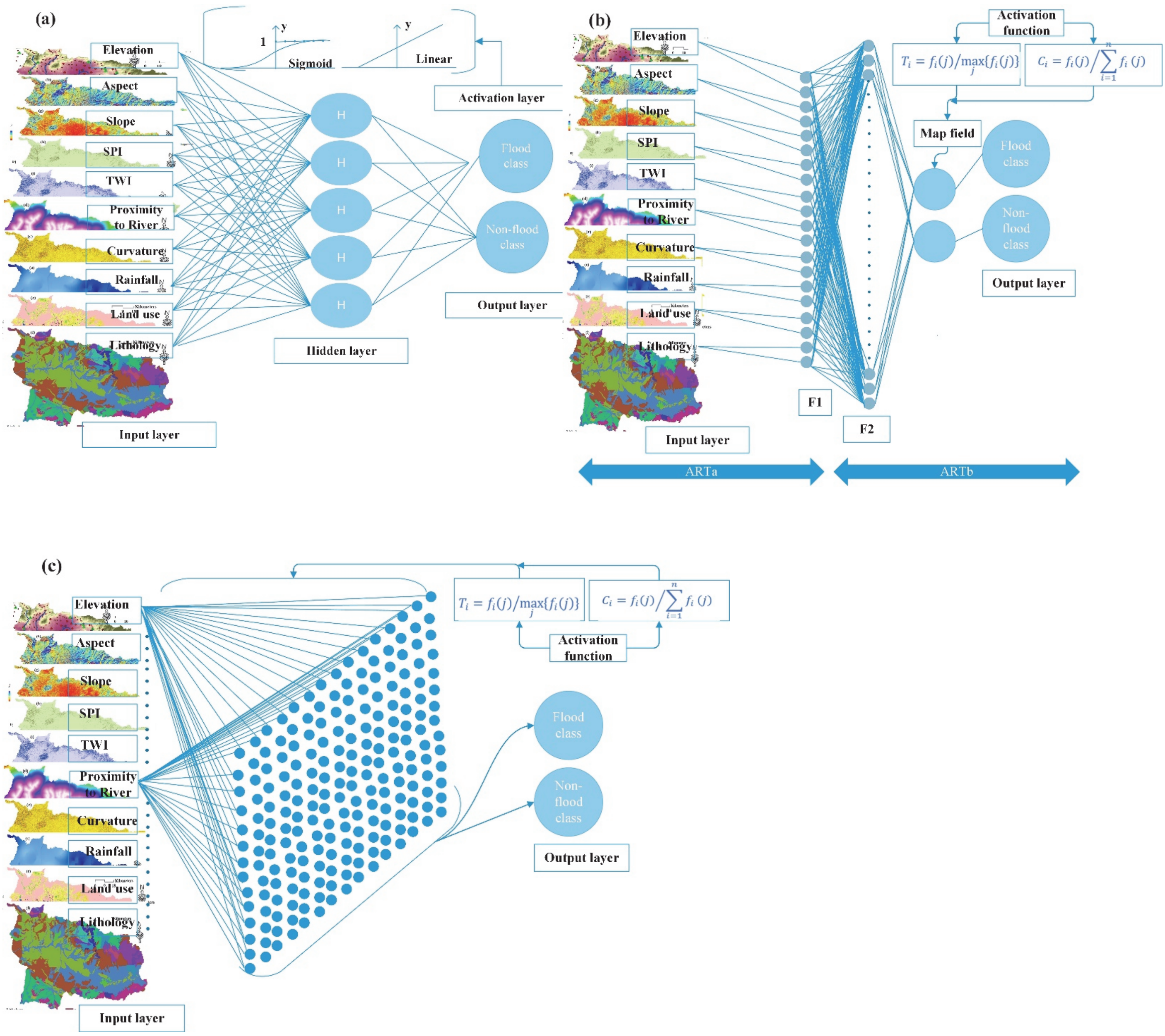

(a)
Elevation
Aspect
Slope
SPI
TWI
Proximity to River
Curvature
Rainfall
Land use
Lithology
Input layer
Sigmoid
Linear
Activation layer
H
Hidden layer
Flood class
Non-flood class
Output layer
(b)
Activation function
$T_i = f_i(j)/\max_j\{f_i(j)\}$
$C_i = f_i(j)/\sum_{i=1}^{n} f_i(j)$
Map field
F1
F2
ARTa
ARTb
(c)
Activation function

Fig. 5.

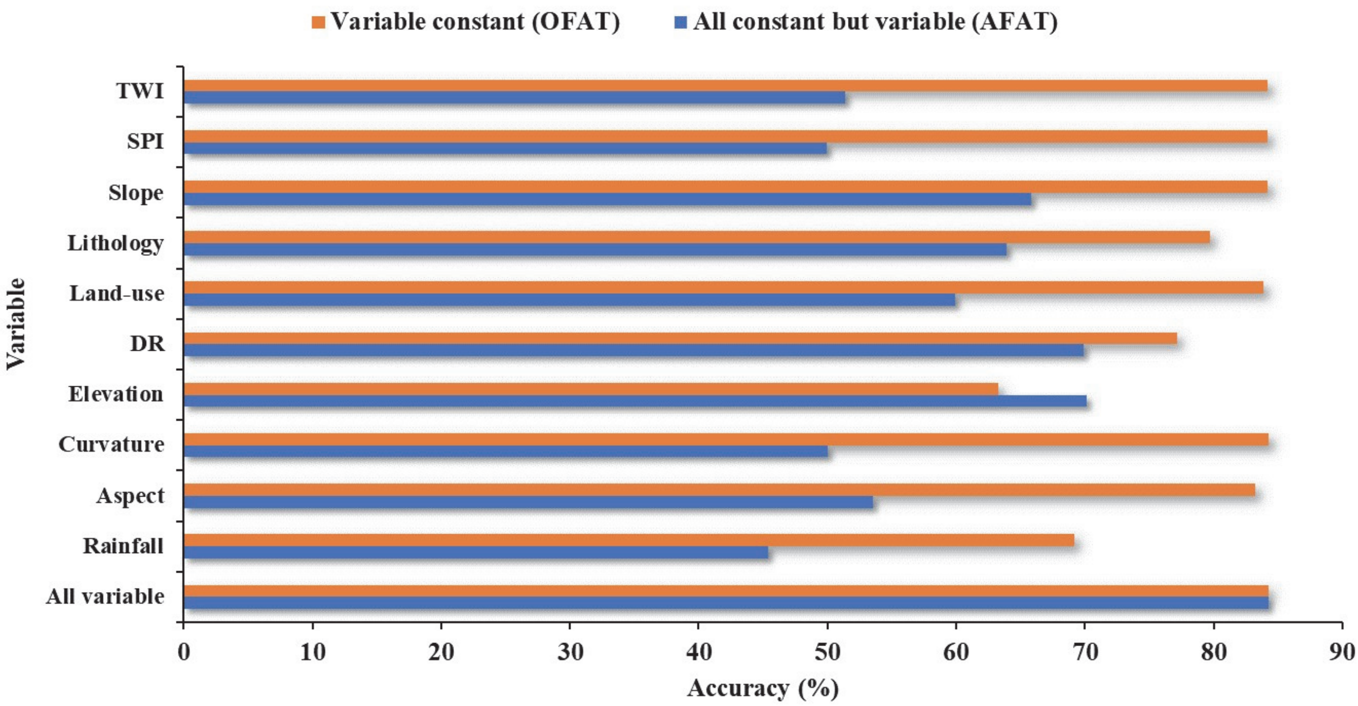

Variable constant (OFAT)
All constant but variable (AFAT)
TWI
SPI
Slope
Lithology
Land-use
DR
Elevation
Curvature
Aspect
Rainfall
All variable
Variable
0
10
20
30
40
50
60
70
80
90
Accuracy (%)

Fig. 6.

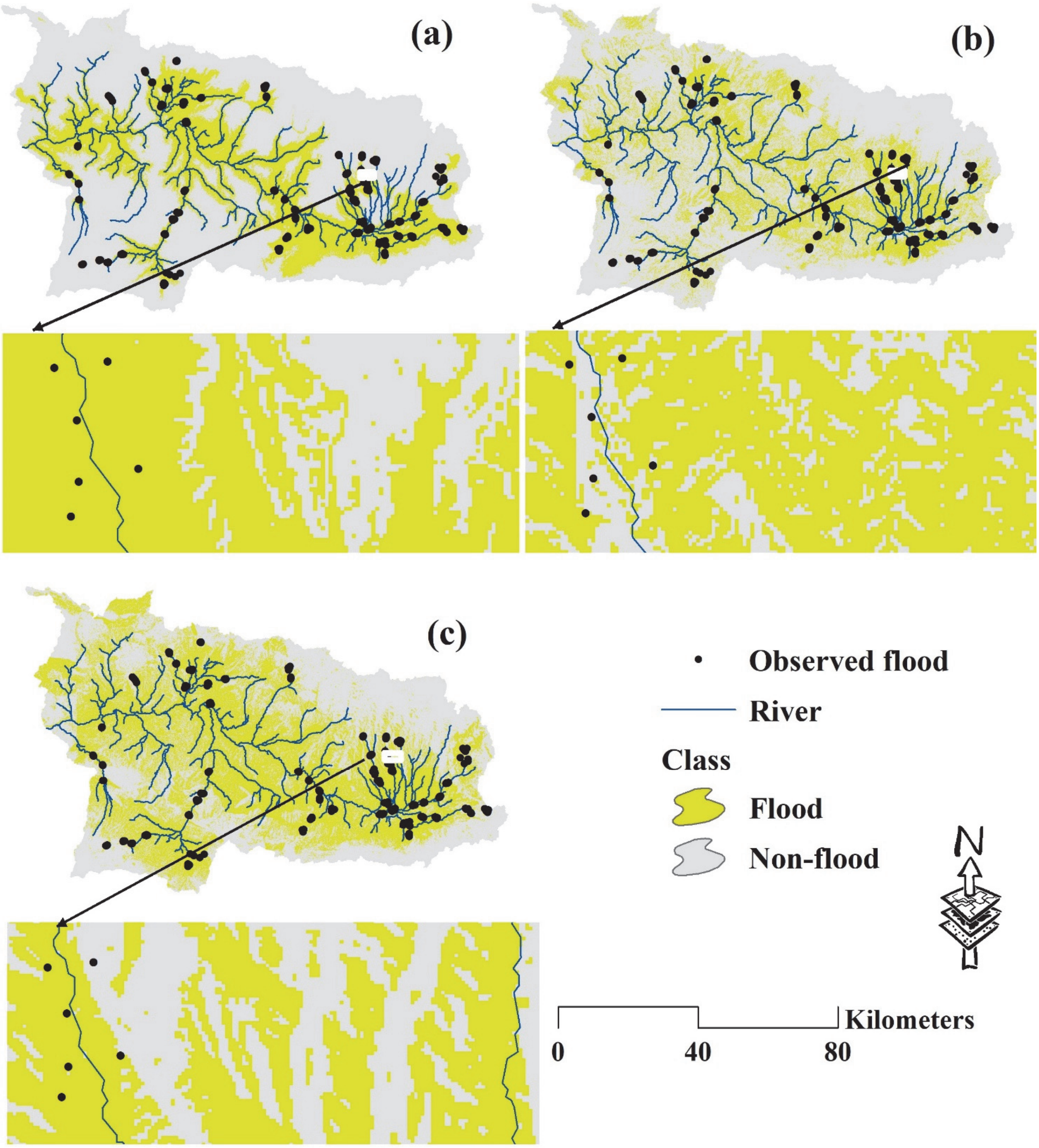
(a)
(b)
(c)
Observed flood
River
Class
Flood
Non-flood
N
0
40
80
Kilometers

Fig. 7.

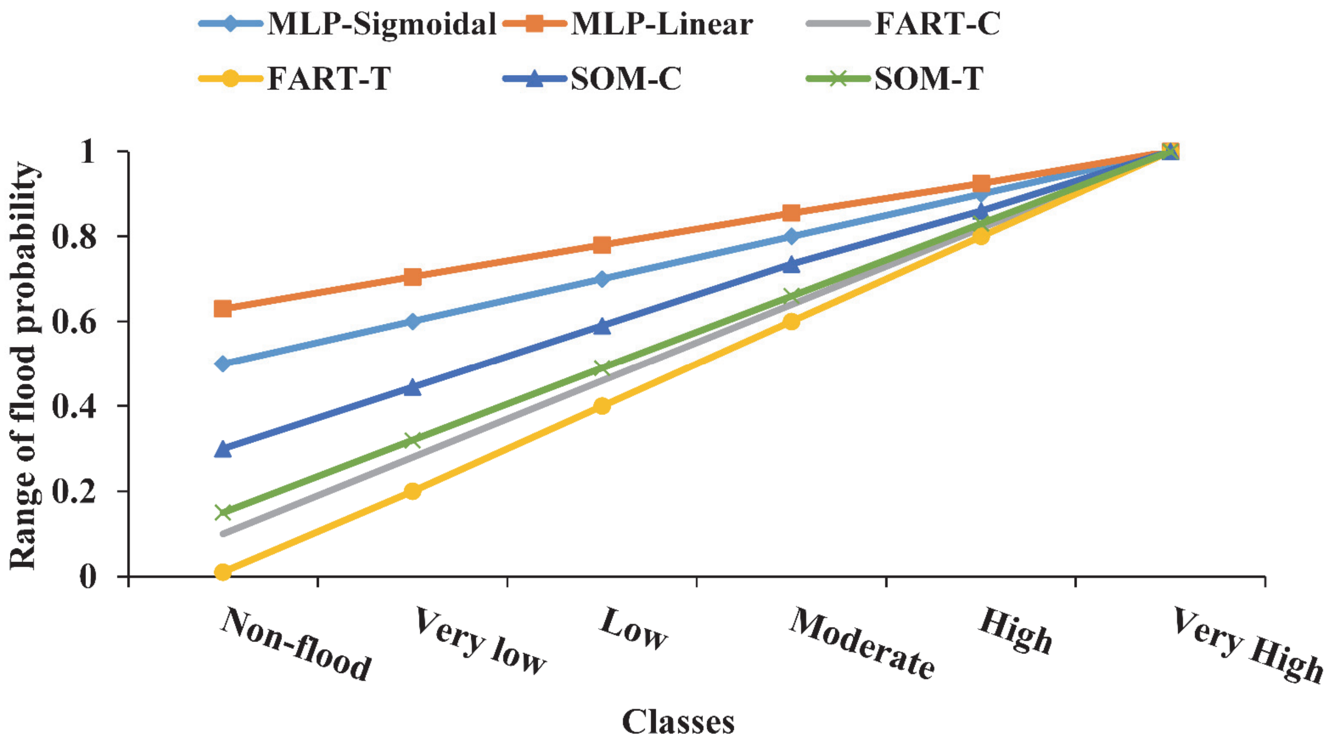
MLP-Sigmoidal
MLP-Linear
FART-C
FART-T
SOM-C
SOM-T
Range of flood probability
1
0.8
0.6
0.4
0.2
0
Non-flood
Very low
Low
Moderate
High
Very High
Classes

Fig. 8.

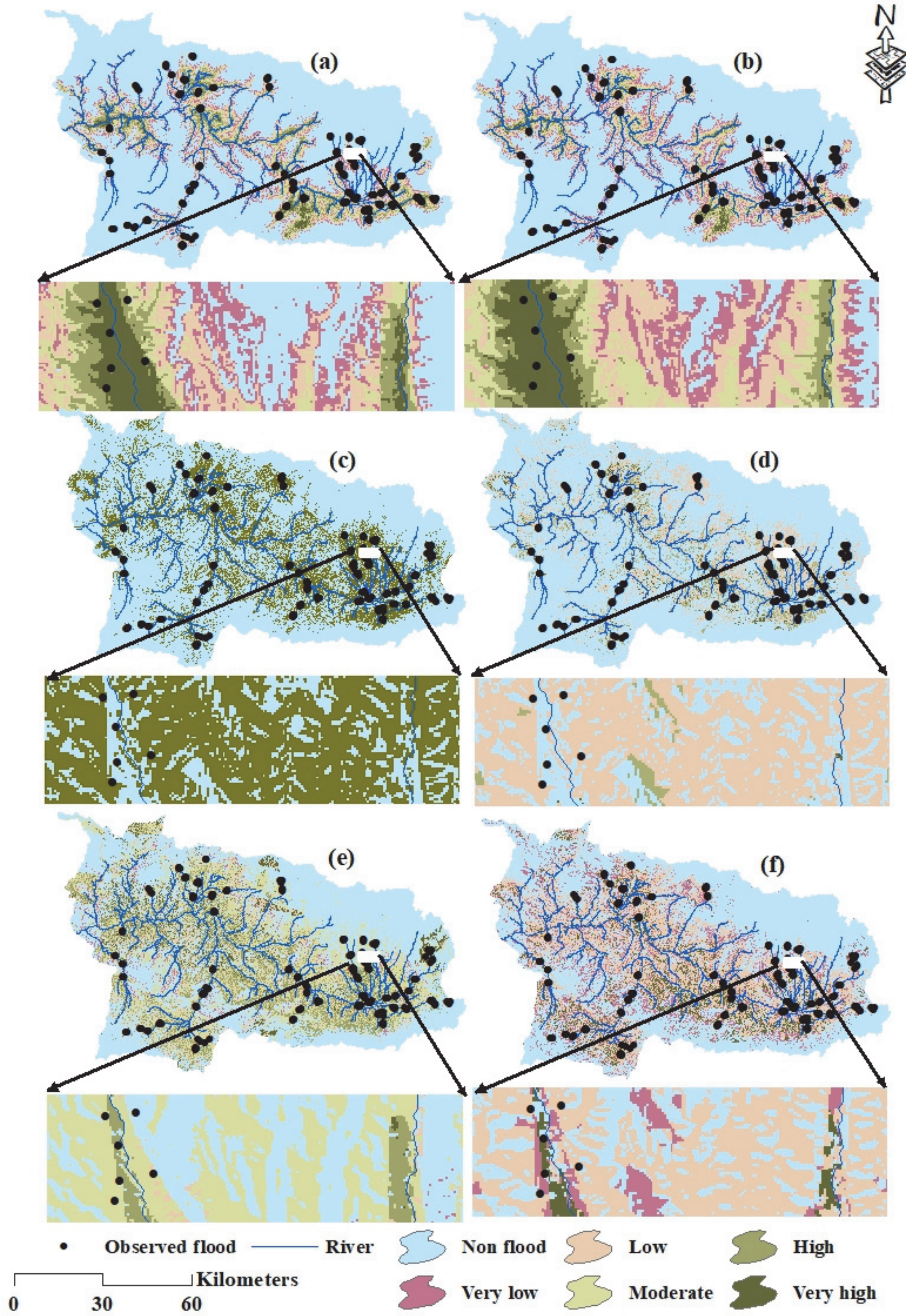
(a)
(b)
(c)
(d)
(e)
(f)
N
Observed flood
River
Non flood
Low
High
Very low
Moderate
Very high
Kilometers
0
30
60

Fig. 9.

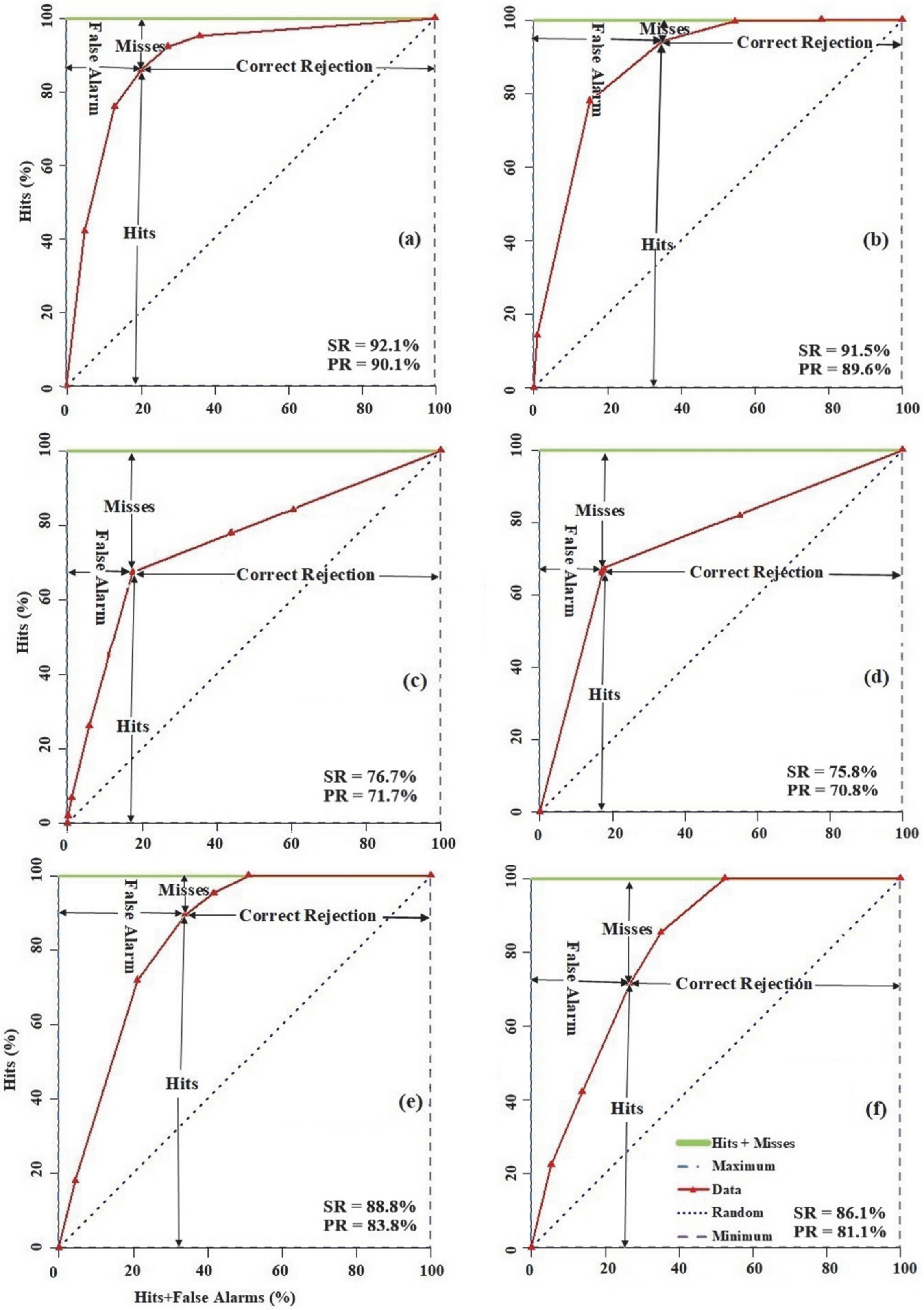

Hits (%)
False Alarm
Misses
Correct Rejection
Hits
(a)
SR = 92.1%
PR = 90.1%
(b)
SR = 91.5%
PR = 89.6%
(c)
SR = 76.7%
PR = 71.7%
(d)
SR = 75.8%
PR = 70.8%
(e)
SR = 88.8%
PR = 83.8%
(f)
SR = 86.1%
PR = 81.1%
Hits + Misses
Maximum
Data
Random
Minimum
Hits+False Alarms (%)

Fig. 10.